Flow dynamics analysis and heat transfer of air jets on metallic foams

Erany D. G. Constantino[1], José L. C. F. Grilo[2], Senhorinha F. Teixeira[3], José Carlos Teixeira[4], Hélder Jesus Puga[5], Flávia Viera Barbosa[6]

*[1] MEtRICs, Department of Mechanical Engineering, University of Minho, Guimarães, Portugal, id9409@alunos.uminho.pt, **CA***
[2] CMEMS, Department of Mechanical Engineering, University of Minho, Guimarães, Portugal, id8983@alunos.uminho.pt
[3] ALGORITMI R&D Centre, Department of Production Systems, University of Minho, Guimarães, Portugal, st@dps.uminho.pt
[4] MEtRICs, Department of Mechanical Engineering, University of Minho, Guimarães, Portugal, jt@dem.uminho.pt
[5] CMEMS, Department of Mechanical Engineering, University of Minho, Guimarães, Portugal, puga@dem.uminho.pt
[6] INEGI - Instituto de Ciência e Inovação em Engenharia Mecânica e Engenharia Industrial, Porto, Portugal, fbarbosa@inegi.up.pt

Abstract

Open-cell metallic foams have gained significant attention in thermal engineering due to their ability to enhance heat transfer through increased surface area and improved fluid–solid interaction. When combined with jet impingement, additional enhancement mechanisms arise from the interaction between the jet flow structures and the porous matrix, leading to intensified mixing and higher local heat transfer rates. However, the coupled effects of jet turbulence, flow penetration within the porous structure, and solid–fluid interaction result in complex flow fields that are not yet fully understood. In this study, the flow behavior and heat transfer performance of an air jet impinging on metallic foams with different porosities and permeabilities are experimentally investigated. A two-dimensional Particle Image Velocimetry (2D-PIV) system was employed to characterize the velocity field, while a heat flux sensor was used to quantify the heat transfer from a heated surface through the porous media. Five aluminum open-cell metallic foams were analyzed to assess the influence of morphological properties on flow and thermal performance.

The results demonstrate that increasing permeability reduces flow resistance and promotes deeper jet penetration into the porous structure, as evidenced by the PIV measurements, which reveal enhanced flow development and internal mixing. These flow features are consistent with the heat transfer results, where higher Nusselt numbers were obtained for more permeable foams. The interaction between the impinging jet and the porous matrix significantly alters the flow field, intensifying fluid–solid interaction and improving convective heat transfer performance. These findings reveal the existence of a permeability threshold governing the transition between porous-dominated and jet-dominated flow regimes, as well as a saturation behavior at high permeability where the porous medium becomes effectively transparent to the impinging jet. Furthermore, the direct relationship between flow structure and heat transfer performance is established, providing a comprehensive basis for the design and optimization of metallic foam-based thermal systems.

Keywords: Flow dynamics; Heat transfer; Jet impingement; Metallic foams; Particle image velocimetry.

1. Introduction

Jet impingement is widely recognized as an effective cooling technique for thermal management applications due to its ability to generate high local convective heat transfer coefficients and maintain reduced surface temperatures with precise spatial control [1,2]. In this approach, a fluid jet is discharged from a nozzle and directed toward a target surface, where the impingement process enhances momentum transfer, promotes strong mixing, and disrupts thermal boundary layers, resulting in efficient heat removal.

Open-cell metallic foams are porous materials composed of three-dimensional networks of interconnected ligaments, forming continuous pathways that allow fluid to permeate the structure [3]. Their high specific surface area increases the interaction between the fluid and solid phases, while the complex internal geometry promotes both momentum and thermal exchange within the porous matrix [4,5].

The thermo-hydraulic performance of metallic foams is strongly governed by their morphological properties. Porosity, defined as the volumetric fraction of void space, controls fluid storage and transport characteristics [6]. Pore density, typically expressed in pores per inch (PPI), describes the distribution of pores within the structure and is directly related to its internal architecture [7]. Permeability, which depends on pore size, porosity, and pore density, quantifies the ease with which the fluid flows through the porous medium [6]. In laminar flow conditions, transport within porous media is predominantly governed by viscous effects, as described in classical models for incompressible flow through porous structures [8]. These parameters are intrinsically coupled and jointly determine the heat transfer behavior of metallic foams [9]. Increasing pore density generally leads to a denser ligament network and smaller pore sizes, which enhances the available surface area for heat exchange but reduces permeability and increases flow resistance [10]. Conversely, higher porosity facilitates fluid penetration and reduces pressure losses, although it may limit the effective heat transfer area [11]. As a result, the thermal performance of metallic foams is governed by a balance between flow accessibility and surface area availability [10,11,12].

The combination of jet impingement with metallic foams has emerged as a promising approach to further enhance heat transfer performance. The impinging jet provides high momentum and localized cooling, while the porous structure promotes flow redistribution, increases fluid–solid interaction, and intensifies internal mixing.

However, the simultaneous influence of jet turbulence, flow penetration within the porous matrix, and solid–fluid coupling results in highly complex flow fields that are not yet fully characterized, posing significant challenges for both experimental investigations and numerical modeling. In this context, the present study investigates the flow behavior and heat transfer performance of an air jet impinging on metallic foams with different porosities and permeabilities. Two-dimensional Particle Image Velocimetry (2D-PIV) was employed to capture the velocity field of the flow, while a heat flux sensor was used to quantify the heat transferred from a heated surface to the air through the metallic foams.

This work provides detailed insight into the interaction between impinging jet flow structures and porous media, highlighting the role of foam morphology in governing flow penetration, mixing mechanisms, and heat transfer performance. The results contribute to a better understanding of the coupled thermo-fluid behavior and support the design and optimization of advanced cooling systems based on metallic foams.

2. Materials and Methods

2.1 Experimental setup

The experimental facility consists of an acrylic flow system supplied by a centrifugal fan, which delivers ambient air to a plenum chamber located at the inlet of a square-section acrylic duct. The plenum acts as a flow conditioning unit, promoting uniform velocity distribution and reducing turbulence intensity. A honeycomb flow straightener is installed upstream of the duct to further improve flow uniformity. At the outlet of the duct, interchangeable elements were used depending on the experimental configuration. For PIV measurements, a custom-designed PLA structure incorporating a circular orifice was mounted, along with a support for the target samples. For heat transfer experiments, this structure was replaced by a metallic plate containing a circular orifice. In both configurations, the orifice diameter and the distance to target surface were kept constant $D = 5\ \mathrm{mm}$ and $H = 10\ \mathrm{mm}$, ensuring consistency between flow visualization and thermal measurements. The airflow exiting the orifice forms a round jet impinging on the target surface positioned downstream. A photographic and schematic representation of the experimental setup is shown in Fig. 1 a and b.

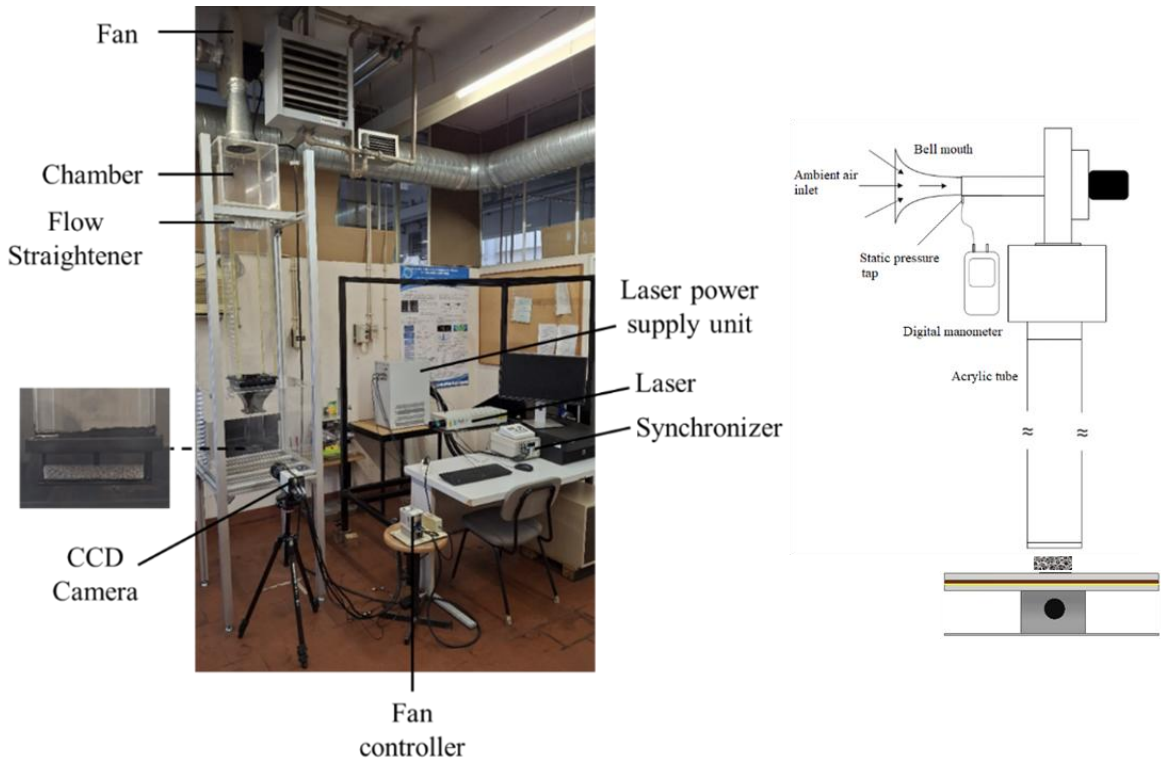

(a) (b)

Figure. 1. *Experimental setup: a) photograph of the experimental facility for PIV measurements, b) schematic representation of the experimental setup for heat transfer measurements.*

2.2 Target surfaces

Five metallic foams and one solid sample were used as a target surfaces in the PIV experiments, while only metallic foams were considered in the heat transfer experiments. The foams differ in porosity and permeability. The structure of the samples is presented in table 1.

Table 1. Target surfaces characteristics.

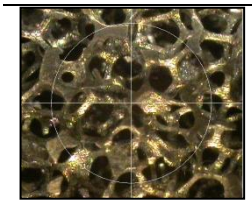	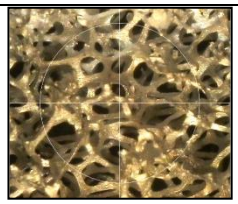	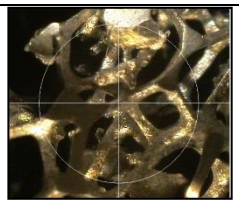	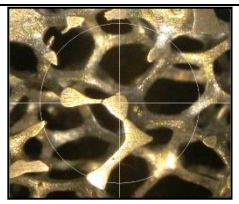	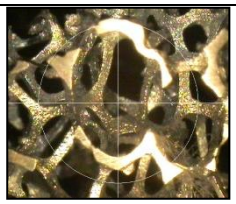	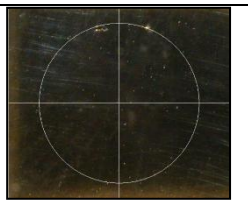
Foam 1	Foam 2	Foam 3	Foam 4	Foam 5	Solid
Porosity ε, %					
79	82	90	91	92	-
Permeability K, m^2					-
$9.31 \cdot 10^{-9}$	$9.98 \cdot 10^{-9}$	$2.44 \cdot 10^{-8}$	$2.46 \cdot 10^{-8}$	$2.54 \cdot 10^{-8}$	-
Inertial coefficient F, m^{-1}					-
1766.09	1766.96	1099.95	1110.87	1182.16	-

2.3 Measurements techniques

2.3.1 PIV measurements

The velocity field was characterized using a Particle Image Velocimetry (PIV) system based on a double-pulse laser source. The emitted coherent beam was shaped into a thin laser sheet using a cylindrical lens, allowing the illumination of a two-dimensional plane within the seeded flow. Two successive light pulses were used to illuminate the tracer particles, and the scattered light was recorded by a CCD camera. The acquisition process was controlled by an electronic synchronizer, ensuring that one image was captured after each laser pulse. Image acquisition was performed in double-frame mode, in which a single frame is recorded for each trigger signal. The time interval between the two laser pulses defines the effective exposure time, and the camera is triggered twice to capture two consecutive particle images, resulting in a double-exposure dataset [13].
Velocity vectors were obtained using a cross-correlation of image pairs. In the present study, the trigger rate was fixed at the maximum allowable frequency of the laser system $(15\ \mathrm{Hz})$ [14]. While the instantaneous velocity is primarily determined by particle displacement and Δt. Prior to the experiments, the PIV system was calibrated using a reference scale to establish the spatial resolution. Additional validation procedures were carried out to ensure measurement reliability, including verification of particle seeding quality (size, concentration, and distribution), adjustment of the laser sheet thickness and intensity, and alignment of the laser sheet with the jet outlet and the porous surface. The CCD camera (Hysense Zyla) was positioned perpendicular to the laser sheet to minimize optical distortion. The optimal pulse separation time was determined experimentally based on the flow regime.

2.3.2 Heat transfer measurements

Convective heat transfer was quantified using a thin-film heat flux sensor (HFS-4, OMEGA®) mounted at the center of an aluminum heating plate $(200 \times 200 \times 5\ mm)$. A uniform thermal contact was ensured by applying a thin and uniform layer of Thermalright TFX thermal paste between the sensor and the plate. Uniform heating of the aluminum plate was achieved using a $1000\ W$ electrical heater $(200 \times 200\ mm)$, positioned between two supporting plates and the aluminum plate. The plate temperature was controlled using a Selec TC544 temperature controller operating in on–off mode. A type K thermocouple was mounted in the aluminum plate to monitor the local temperature and provide feedback to the controller. The heat flux sensor includes an integrated type K thermocouple for local temperature measurement. In addition, three type K thermocouples were installed within the metallic foams to monitor their temperature, while an extra thermocouple was attached to the aluminum plate to validate the temperature readings provided by the control system. All thermocouples, together with the heat flux sensor, were connected to a National Instruments NI 9213 data acquisition system. Data acquisition and processing were performed using a LabVIEW-based software platform. Photograph of the experimental setup is presented in Fig. 2.

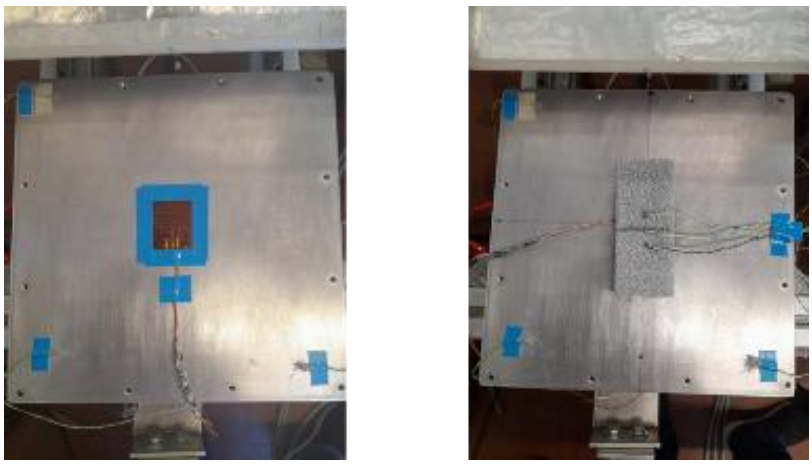

(a) (b)

Figure. 2. *Heat transfer experimental setup: a) aluminum heat plate and heat flux sensor, b) aluminum heat plate and metallic foam.*

The heat flux sensor measures heat flux based on the temperature gradient across a known thermal resistance [2]. The heat flux is determined using Fourier's law of heat conduction, expressed as Eq. (1):

$$\bar{q} = -k\left(\frac{\Delta T}{\Delta x}\right) \quad (1)$$

where the temperature difference ΔT, is measured across a Kapton® layer of thickness $\Delta x = 0.38\,mm$ and thermal conductivity $k = 0.045\ W/mK$, according to manufacturer specifications.
The average convective heat transfer coefficient, $\bar{h}$, was calculated as:

$$\bar{h} = \frac{\bar{q}}{(\overline{T_w} - \overline{T_j})} \quad (2)$$

where $\bar{q}$ is the average heat flux measured by the sensor, T_w is the average temperature of the aluminum plate, and T_j corresponds to the jet air temperature.
The corresponding average Nusselt number was obtained from Eq. (3):

$$\overline{\mathrm{Nu}} = \frac{\bar{h}\,D}{k} \quad (3)$$

where D represents the nozzle diameter and k is the thermal conductivity of air, evaluated at the jet temperature. The jet temperature was assumed equal to the ambient temperature for the evaluation of air thermophysical properties.

2.4 Seeding generator and seeding particles

In the present study, air was used as the working fluid. Seeding was generated using a Concept Smoke Systems Aerotech Smoke Wand, which produces particles through the thermal vaporization of a non-toxic white oil. The oil is delivered to the probe tip by a peristaltic pump and vaporized by a low-voltage heating element, generating a dense and stable aerosol. The probe is aerodynamically designed to minimize flow disturbance during injection. Two operating parameters can be adjusted: the oil flow rate and the heating voltage. These control the amount of oil supplied and the vaporization temperature, respectively, thereby influencing particle concentration and size distribution. Appropriate tuning of these parameters is required to ensure adequate seeding density while maintaining good flow tracking capability. The measurement of particle size and concentration was previously performed by Erany et al. [15]. In the present work, the operating parameters were $15\ \mathrm{V}$ with an oil flow rate of 5, ensuring appropriate particle size and seeding density for reliable image acquisition and accurate velocity field determination.

2.5 Experimental conditions

All experiments were conducted at an ambient temperature of $20\ °C$ and atmospheric pressure. Air properties were considered as: density $\rho = 1.204\ \mathrm{kg/m^3}$, dynamic viscosity $\mu = 1.825x10^{-5}\ \mathrm{kg/m \cdot s}$, and thermal conductivity $k = 0.02514\ \mathrm{W/m.K}$. [16].
The flow velocity at the jet outlet was measured using a Pitot tube, and the Reynolds number was calculated based on jet exit conditions:

$$Re = \frac{\rho V_j D}{\mu} \quad (4)$$

The operating conditions for PIV and heat transfer experiments are summarized in Tables 2 and 3.

TABLE 2. Experimental conditions for PIV measurements.

Single jet			**Fluid runoff**		**PIV**		
Fan Frequency	Flow Velocity m/s	Reynolds number	Regime	Time between pulses (μs)	Laser 1 (volts)	Laser 2 (volts)	Repetition
3.3	4.2	1400	Laminar	250	8	8	6
7.0	9.1	3000	Transition	100	8	8	6
11.9	15.1	5000	Turbulent	50	8	8	6

TABLE 3. Experimental conditions for heat transfer measurements.

Single jet			
Fan frequency	Flow velocity m/s	Re	Fluid runoff
3.3	4.2	1400	Laminar
7.0	9.1	3000	Transition
11.9	15.1	5000	Turbulent
30	38.2	12,000	Full turbulent

2.6 Experimental procedure

For the PIV measurements, the experimental procedure began with the alignment of the laser sheet with the jet outlet of the PLA structure. The Hisense Zyla CCD camera was positioned perpendicular to the laser sheet. Prior to image acquisition, the system was calibrated to establish the spatial scale. A graduated ruler was placed at the location of the target surface support, aligned with the laser sheet plane, and an image was recorded for calibration purposes. The calibration procedure consisted of defining two reference points (A and B) in the captured image corresponding to a known physical distance. After calibration, the ruler was removed and the first target surface was positioned at a distance of 10 mm from the jet outlet, aligned with the laser sheet. The seeding particle generator was then activated, allowing sufficient time for the particles to uniformly disperse within the acrylic duct. Once adequate seeding density was achieved, the fan was operated under laminar flow conditions. Image acquisition was initiated as soon as the seeded flow became clearly visible, and the recorded images were stored for subsequent processing.

For the heat transfer measurements, the metallic foam sample was placed directly on the heat flux sensor at a distance of 10 mm from the jet outlet, and the heating system was activated. Heat flux, foam temperature, air jet temperature, and heating surface temperature were initially monitored under natural convection conditions until steady state was achieved, corresponding to a heat flux of approximately 700 W/m². Subsequently, the fan was activated to generate an air jet under laminar flow conditions, and the same variables were recorded over a period of 30 minutes. The procedure was then repeated for all flow regimes considered in the study. Throughout the experiments, key geometric parameters namely the nozzle diameter, the nozzle-to-surface spacing, and the positioning of the metallic foam were kept constant to ensure direct comparability between test conditions. To assess measurement repeatability, each experiment was performed three times for every sample. The maximum observed variation was approximately 5% for heat flux measurements and 8% for temperature measurements.

2.7 Uncertainty analysis

Uncertainties in the PIV measurements may arise from several sources, including calibration errors, timing inaccuracies, optical misalignment, particle lag, as well as image processing limitations such as interrogation window selection and background noise. These sources can be broadly classified into systematic and random errors. Systematic uncertainties are primarily associated with calibration procedures, optical setup, and the selection of appropriate seeding particles and pulse separation time. In the present study, these effects were minimized through careful calibration, alignment of the optical components, and optimization of the experimental parameters.

The uncertainty analysis focused on the quantification of the random component of the velocity measurement uncertainty. This component is mainly related to the image acquisition and processing stages, including particle image quality, cross-correlation performance, and interrogation window definition. The random uncertainty was estimated following the methodology described in [13], resulting in an uncertainty of approximately 5% for the measured velocity field.

The combined random uncertainty was evaluated assuming independence between the two in-plane velocity components, and calculated as:

$$\sigma_R = \sqrt{\sigma_U^2 + \sigma_V^2} \tag{5}$$

where σ_U and σ_V represent the standard uncertainty associated with the horizontal and vertical velocity components, respectively.

It should be noted that the reported uncertainty refers to the random component of the velocity measurements. Systematic uncertainties were not explicitly quantified but were mitigated through experimental design and calibration procedures.

The uncertainty associated with the heat transfer measurements was estimated from the instrumental uncertainties of the heat flux sensor, thermocouples, and nozzle diameter. The uncertainties considered were $\pm 0.577\ W/m^2$ for the heat flux sensor, $\pm 0.115\ °C$ for the thermocouples, and $\pm 0.011\ mm$ for the nozzle diameter following approach used by [17]. The convective heat transfer coefficient uncertainty was obtained by standard uncertainty propagation from heat flux and temperature difference measurements as expressed in Eq. 6. The Nusselt number uncertainty was obtained by propagating the uncertainties of the heat transfer coefficient and nozzle diameter Eq. 7.

$$u_h = h\sqrt{\left(\frac{u_q}{q}\right)^2 + \left(\frac{u_{\Delta T}}{T_w - T_j}\right)^2} \tag{6}$$

where $u_q, u_{\Delta T}$, represent the uncertainties of the heat flux and temperature difference respectively.

$$u_{NU} = Nu\sqrt{\left(\frac{u_h}{h}\right)^2 + \left(\frac{u_D}{D}\right)^2} \tag{7}$$

where u_h and u_D represent uncertainties of heat transfer coefficient and nozzle diameter.

Since the jet temperature was assumed equal to the ambient temperature, the uncertainty in the temperature difference was taken as the thermocouple uncertainty associated with the wall temperature measurement.

The uncertainty analysis showed that the instrumental uncertainty of the heat transfer measurements was small compared with the magnitude of the measured quantities. The relative uncertainty of the heat transfer coefficient was approximately $0.15 - 0.17\%$, while the relative uncertainty of the Nusselt number was approximately $0.27 - 0.28\%$, depending on the operating condition. However, these values do not account for variability associated with experimental conditions. Although the instrumental uncertainties were found to be low, the experimental repeatability exhibited variations of approximately 5% for heat flux and 8% for temperature. These deviations are attributed to inherent fluctuations in the experimental setup and operating conditions and are therefore considered representative of the overall experimental uncertainty.

3. Results and Discussion

3.1 Particle image velocimetry

The flow field obtained from Particle Image Velocimetry (PIV) measurements provides detailed insight into the interaction between the impinging jet and metallic foams. The analysis considers velocity magnitude, turbulence intensity, and vorticity, enabling the identification of dominant flow mechanisms under varying Reynolds numbers and foam morphologies. Results are discussed according to the flow regime, emphasizing the roles of permeability (K) and inertial coefficient (F) in shaping the flow structure.

In the laminar regime, the flow is governed by viscous effects, with permeability controlling the interaction with the porous medium [8]. For the solid surface, the jet remains coherent, with a well-defined axial core and limited lateral spreading. Vorticity is confined to shear layers and the impingement region, and turbulence intensity remains low. In the foams, permeability strongly influences the flow. The lowest permeability case (Foam 1) induces significant disturbances, including velocity fluctuations, increased vorticity, and loss of jet coherence near the interaction region, due to high flow resistance. As permeability increases (Foams 2–5), jet coherence is progressively restored, turbulence intensity decreases, and vorticity becomes more organized. For high-permeability foams, the flow approaches the behavior observed over the solid surface.

In the transitional regime, both viscous and inertial effects contribute to the flow dynamics, leading to more complex interactions. The solid surface exhibits increased turbulence intensity and more pronounced vorticity, particularly in the wall jet region. Foam morphology plays a key role in this regime. Foam 1 promotes strong destabilization, with high turbulence intensity and diffuse vorticity, indicating early transition and enhanced

mixing. Foam 2 shows partial recovery of the jet, although turbulence remains elevated. For higher permeability foams (Foams 3–5), the jet becomes well-defined, turbulence intensity decreases, and vorticity structures are confined to classical regions. This behavior suggests the existence of a permeability threshold beyond which the porous medium no longer dominates the flow. In this regime, both K and F are relevant, with inertial effects becoming increasingly important for low-permeability foams.
In the turbulent regime, inertial effects dominate, and the inertial coefficient (F) governs the flow behavior. Over the solid surface, the jet exhibits a fully developed turbulent structure, with a strong axial core, high turbulence intensity, and well-defined vorticity. Low-permeability foams (Foams 1–2) strongly disrupt the flow, leading to loss of jet coherence, high and spatially distributed turbulence, and diffuse vorticity, indicating amplified instabilities and enhanced mixing. As permeability increases (Foams 3–5), the jet structure is progressively restored, with improved coherence and penetration. Turbulence becomes more organized, and vorticity is confined to shear layers and the impingement region. For high-permeability foams, the flow closely resembles that of the solid surface, indicating limited influence of the porous medium.

3.1.1 Cross-analysis: effect of K, F and Re

A combined analysis of all regimes reveals a clear transition in the governing mechanisms.
In the laminar regime, the flow is dominated by viscous effects, with permeability (K) as the main controlling parameter. Low-permeability foams disrupt the jet, while high-permeability foams allow near-undisturbed flow.
In the transitional regime, both permeability and inertial effects influence the flow. A critical permeability threshold separates regimes dominated by the porous medium from those where the jet structure is preserved.
In the turbulent regime, the flow is dominated by inertial effects, with the inertial coefficient (F) as the key parameter. Low-permeability foams amplify turbulence and promote chaotic structures, whereas high-permeability foams yield organized flow similar to the solid case.
Additionally, a saturation behavior is observed for high-permeability foams (Foams 3–5), where further increases in permeability do not significantly alter the external flow field, indicating that the porous medium becomes effectively transparent to the impinging jet.

3.2 Heat transfer

The variation of the average Nusselt number with Reynolds number for all metallic foams is shown in Fig. 3. The results are discussed according to the main governing factors affecting heat transfer.

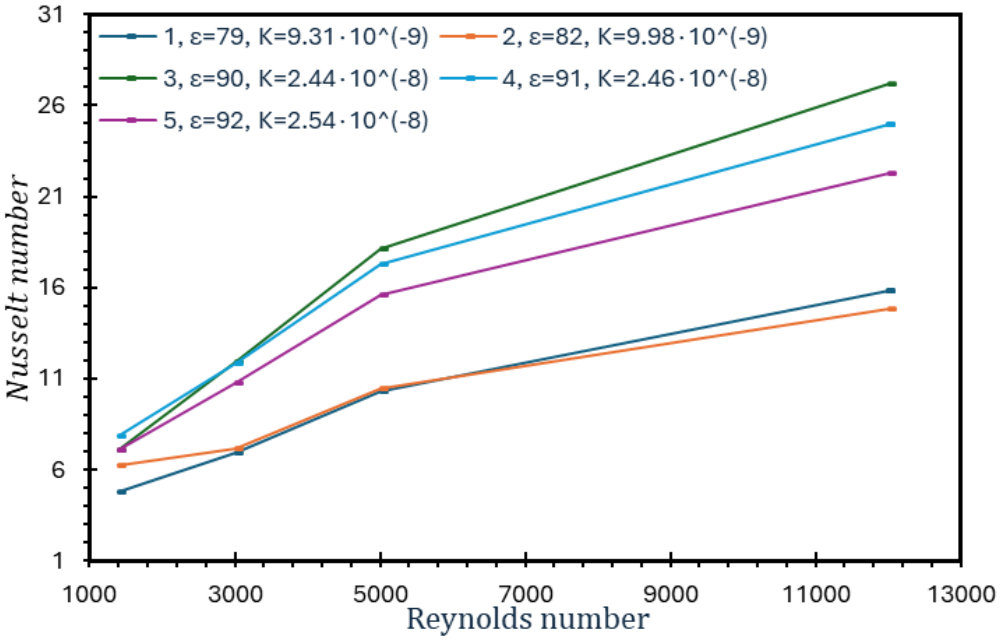

Figure. 3. *Nusselt number as function of Reynolds, single jet impingement.*

3.2.1. Effect of Reynolds number

The Nusselt number increases systematically with Reynolds number for all metallic foams. This trend is consistent with [17,18,19]. Differences between foam structures become more pronounced at higher Reynolds numbers, the gap between best and worst cases rises from 3.07 in the laminar regime to 12.4 under fully turbulent conditions. This trend indicates that the influence of the porous structure intensifies with increasing flow momentum, as the jet penetrates deeper into the foam and enhances internal mixing. At low Reynolds numbers, the flow lacks sufficient energy to fully exploit structural differences, whereas at higher values the jet–foam interaction dominates the thermal response

3.2.2. Influence of foam morphology

Heat transfer performance strongly depends on foam morphology, particularly the combined effects of porosity, permeability, and inertial resistance. Foams 1 and 2, characterized by lower porosity and permeability, exhibit the lowest Nusselt numbers across most conditions. In contrast, Foams 3–5 achieve significantly higher values, especially in the transitional regime, these results are consistent with those reported by Calmidi et al. [21] and Shih et al. [22].

3.2.3. Non-monotonic effect of porosity

Heat transfer enhancement does not increase monotonically with porosity. Although Foam 5 has the highest porosity (92%) and permeability ($2.54 \cdot 10^{-8}\ m^2$), its Nusselt number remains lower than that of Foam 3 and, in many cases, Foam 4. This behavior reflects a balance between flow penetration, mixing intensity, and available heat transfer surface area. Highly porous structures facilitate flow passage but may reduce thermal interaction if internal surface area or flow disturbance is insufficient. This result highlights a trade-off between porosity and pore density (PPI). While higher porosity reduces hydraulic resistance and promotes penetration, higher pore density increases surface area and enhances mixing, particularly at lower Reynolds numbers.
Consequently, thermal performance depends on the balance between these competing effects, which varies with flow regime, in accordance with results reported by [9]. The optimal combination of porosity and pore density should therefore be selected according to the thermal and hydraulic requirements of the application.

3.2.4. Optimal configuration

Foam 3 provides the best overall thermal performance from transitional to fully turbulent regimes, while Foam 4 achieves the highest Nusselt number only in laminar conditions. These results indicate that Foam 3 offers an optimal balance between porosity, pore density, permeability, and inertial resistance, maintaining strong internal surface interaction without excessive flow resistance. Foam 4 exhibits similar behavior, suggesting that both structures are close to an optimal morphological configuration for heat transfer enhancement.

Conclusions

This study investigated the flow dynamics and heat transfer performance of an air jet impinging on open-cell metallic foams with different morphologies. The combined use of Particle Image Velocimetry (PIV) and heat flux measurements enabled a detailed characterization of jet–foam interactions across laminar, transitional, and turbulent regimes. The main findings are summarized as follows:

Flow behavior is governed by permeability (K) and inertial coefficient (F). Permeability controls jet penetration and coherence, while the inertial coefficient governs turbulence generation and flow instabilities, with their relative importance depending on the Reynolds number.

Flow regimes strongly influence jet–foam interaction. Laminar flow is dominated by viscous effects, transitional flow involves a balance between viscous and inertial contributions with a critical permeability threshold, and turbulent flow is governed primarily by inertial effects.

Foam morphology significantly affects flow structure. Low-permeability foams (Foams 1–2) enhance mixing but disrupt jet coherence, producing highly unstable flow fields. In contrast, high-permeability foams (Foams 3–5) preserve jet structure and generate more organized flow, approaching solid-surface behavior. A saturation behavior occurs at high permeability. Beyond a critical threshold, further increases in permeability do not significantly affect the flow, indicating that the porous medium becomes effectively transparent to the jet.

Heat transfer is closely linked to flow dynamics. The increase in Nusselt number with Reynolds number reflects enhanced momentum transport and mixing, with foam morphology playing a more significant role at higher Reynolds numbers. Heat transfer does not increase monotonically with porosity. Excessive porosity reduces internal surface area and limits fluid–solid interaction. As a result, Foams 3 and 4 outperform Foam 5, highlighting the need for a balance between permeability and surface area. Optimal performance results from a balance between flow penetration and internal interaction. Foam 3 provides the best overall performance, combining favorable permeability, pore density, and moderate inertial resistance.

Overall, the thermo-fluid performance of metallic foams under jet impingement is governed by the coupled effects of permeability, inertial resistance, and flow regime. The identification of transition and saturation behaviors provides practical guidelines for the design and optimization of foam-based thermal management systems.

Acknowledgements

The first author would like to express his gratitude for support given by the Fundação para a Ciência e Tecnologia (FCT) and the MIT Portugal Program.

This work has been supported by Fundação para a Ciência e Tecnologia (FCT) within PhD Research Fellowship reference PRT/BD/154483/2022, and R&D Units Project Scope: UIDB/04077/2025 (METRICS Center), UID/00319/2025 (ALGORITMI Center), UIDB/04436/2025 (CMEMS).

Nomenclature

Symbol	definition	Unit
2D	Two-dimensional	-
CCD	Charge-Coupled Device	-
D	Nozzle diameter	(m)
F	Inertial coefficient	(m^{-1})
$\bar{h}$	Heat transfer coefficient	$(\mathrm{W/m^2 \cdot K})$
K	Permeability	$(\mathbf{m^2})$
k	Thermal conductivity	$(\mathrm{W/m \cdot K})$

$\overline{\mathrm{Nu}}$	Average Nusselt number	-
PLA	Poly lactic acid	-
PIV	Particle Image Velocimetry	-
$\bar{\mathrm{q}}$	Average heat flux	$(\mathrm{W/m^2})$
Re	Reynolds number	-
T	Temperature	$(°\mathrm{C})$
u	Uncertainty	-
$\mathrm{V_j}$	Jet velocity	(m/s)
Greek Symbol		-
Δt	Triger rate	(Hz)
ε	Porosity	(%)
μ	Dynamic Viscosity	$(\mathrm{kg/m \cdot s})$
ρ	Density	$(\mathrm{kg/m^3})$
σ	Standard deviation	
Subscript		-
j	Jet	-
w	Wall	-

REFERENCES

[1] M. Hefny, J. S. Cotton, and A. Emadi, “The use of pulsating jet impingement to minimize temperature oscillations caused by fluctuating heat-flux boundary conditions,” *Appl. Therm. Eng.*, vol. 258, Jan. 2025, doi: 10.1016/j.applthermaleng.2024.124650.

[2] F. V. Barbosa, S. F. F. C. Teixeira, and J. C. F. Teixeira, “Heat transfer and fluid dynamics of a single jet impingement – An experimental and numerical approach,” *International Journal of Thermal Sciences*, vol. 200, Jun. 2024, doi: 10.1016/j.ijthermalsci.2024.108993.

[3] A. Sutygina, U. Betke, and M. Scheffler, “Manufacturing of Open-Cell Aluminium Foams: Comparing the Sponge Replication Technique and Its Combination with the Freezing Method,” *Materials*, vol. 15, no. 6, Mar. 2022, doi: 10.3390/ma15062147.

[4] E. D. G. Constantino, S. F. C. F. Teixeira, J. C. F. Teixeira, and F. V. Barbosa, “Innovative Solar Concentration Systems and Its Potential Application in Angola,” *Energies (Basel).*, vol. 15, no. 19, p. 7124, Sep. 2022, doi: 10.3390/en15197124.

[5] W. H. Shih, C. C. Liu, and W. H. Hsieh, “Heat-transfer characteristics of aluminum-foam heat sinks with a solid aluminum core,” *Int. J. Heat Mass Transf.*, vol. 97, pp. 742–750, Jun. 2016, doi: 10.1016/j.ijheatmasstransfer.2016.02.044.

[6] R. Ranjbarzadeh and G. Sappa, “Numerical and Experimental Study of Fluid Flow and Heat Transfer in Porous Media: A Review Article,” Feb. 01, 2025, *Multidisciplinary Digital Publishing Institute (MDPI)*. doi: 10.3390/en18040976.

[7] A. Bandyopadhyay, I. Mitra, J. D. Avila, M. Upadhyayula, and S. Bose, “Porous metal implants: processing, properties, and challenges,” Sep. 01, 2023, *Institute of Physics*. doi: 10.1088/2631-7990/acdd35.

[8] S. Liu, A. Afacan, and J. Masliyah’, “STEADY INCOMPRESSIBLE LAMINAR FLOW IN POROUS MEDIA,” May 1994. doi: https://doi.org/10.1016/0009-2509(94)00168-5.

[9] A. Arshad, M. Saeed, M. Ikhlaq, M. Imran, and Y. Yan, “Heat and fluid flow analysis of micro-porous heat sink for electronics cooling: Effect of porosities and pore densities,” *Thermal Science and Engineering Progress*, vol. 57, Jan. 2025, doi: 10.1016/j.tsep.2024.103129.

[10] P. H. Jadhav, T. G, N. Gnanasekaran, and M. Mobedi, “Performance score based multi-objective optimization for thermal design of partially filled high porosity metal foam pipes under forced convection,” *Int. J. Heat Mass Transf.*, vol. 182, Jan. 2022, doi: 10.1016/j.ijheatmasstransfer.2021.121911.

[11] P. H. Jadhav, N. Gnanasekaran, and M. Mobedi, “Analysis of functionally graded metal foams for the accomplishment of heat transfer enhancement under partially filled condition in a heat exchanger,” *Energy*, vol. 263, Jan. 2023, doi: 10.1016/j.energy.2022.125691.

[12] P. H. Jadhav, N. Gnanasekaran, D. A. Perumal, and M. Mobedi, “Performance evaluation of partially filled high porosity metal foam configurations in a pipe,” *Appl. Therm. Eng.*, vol. 194, Jul. 2021, doi: 10.1016/j.applthermaleng.2021.117081.

[13] F. Vieira Barbosa, “Universidade do Minho Escola de Engenharia Convection from Multiple Jets over a Complex Moving Surface,” 2021. Accessed: Jun. 26, 2025. [Online]. Available: https://repositorium.sdum.uminho.pt/handle/1822/75928

[14] “Dantec Dynamics, ‘Dynamic Studio, User’s Guide.,’” 2016, *Skovlunde*.

[15] E. D. G. Constantino, F. V Barbosa, J. L. C. F. Grilo, S. C. F. Teixeira, and J. C. F. Teixeira, “FLOW DYNAMICS ANALYSIS OF AIR JETS ON POROUS SURFACES,” in *Proceedings of the ASME 2025 International Mechanical Engineering Congress and Exposition IMECE2025*, Memphis, Tennessee: ASME IMECE 2025, Nov. 2025. doi: https://doi.org/10.1115/IMECE2025-166585.

[16] Yunus A. Çengel and Michael A. Boles, “Appendix 1 PROPERTY TABLES AND CHARTS (SI UNITS),” 2000.

[17] F. V. Barbosa, S. F. C. F. Teixeira, and J. C. F. Teixeira, “Experimental and numerical study of multiple jets impinging a step surface,” *Energies (Basel)*., vol. 14, no. 20, Oct. 2021, doi: 10.3390/en14206659.

[18] W. H. Hsieh, J. Y. Wu, W. H. Shih, and W. C. Chiu, “Experimental investigation of heat-transfer characteristics of aluminum-foam heat sinks,” *Int. J. Heat Mass Transf.*, vol. 47, no. 23, pp. 5149–5157, Nov. 2004, doi: 10.1016/j.ijheatmasstransfer.2004.04.037.

[19] W. H. Shih, F. C. Chou, and W. H. Hsieh, “Experimental investigation of the heat transfer characteristics of aluminum-foam heat sinks with restricted flow outlet,” *J. Heat Transfer*, vol. 129, no. 11, pp. 1554–1563, Nov. 2007, doi: 10.1115/1.2759972.

[20] J. Wang, H. Kong, Y. Xu, and J. Wu, “Experimental investigation of heat transfer and flow characteristics in finned copper foam heat sinks subjected to jet impingement cooling,” *Appl. Energy*, vol. 241, pp. 433–443, May 2019, doi: 10.1016/j.apenergy.2019.03.040.

[21] V. V. Calmidi and R. L. Mahajan, “Forced convection in high porosity metal foams,” *J. Heat Transfer*, vol. 122, no. 3, pp. 557–565, Aug. 2000, doi: 10.1115/1.1287793.

[22] W. H. Shih, W. C. Chiu, and W. H. Hsieh, “Height effect on heat-transfer characteristics of aluminum-foam heat sinks,” *J. Heat Transfer*, vol. 128, no. 6, pp. 530–537, Jun. 2006, doi: 10.1115/1.2188461.